Journal of Vacuum Science & Technology A

Solid-phase heteroepitaxy of oriented Sb_2Se_3 on GaAs for birefringent thin films

Running title: Solid-phase heteroepitaxy of Sb_2Se_3

Running Authors: Xiao et al.

Kelly Xiao[1,a)], Yuejun Shen[1,2], Arturas Vailionis[3,4], Alec M. Skipper[5], Anna-Katharina Preidl[1], Aaron M. Lindenberg[1,2,6], and Kunal Mukherjee[1,a)]

[1]Department of Materials Science and Engineering, Stanford University, Stanford, CA, 94305, USA
[2]Stanford Institute for Materials and Energy Sciences, SLAC National Accelerator Laboratory, Menlo Park, CA, 94025, USA
[3]Stanford Nano Shared Facilities, Stanford University, Stanford, CA, 94305, USA
[4]Department of Physics, Kaunas University of Technology, Kaunas, Lithuania
[5]Institute for Energy Efficiency, University of California Santa Barbara, Santa Barbara, CA 93106, USA
[6]Stanford PULSE Institute, SLAC National Accelerator Laboratory, Menlo Park, CA 94025, USA

[a)] Electronic mail: kellyx@stanford.edu, kunalm@stanford.edu

We investigate the amorphous-to-crystalline transformation of antimony selenide (Sb_2Se_3) on UHV-prepared GaAs (001) substrates. In the bulk orthorhombic form, Sb_2Se_3 is a layered quasi-1D semiconductor with highly anisotropic properties of interest for optical and electronic devices. We find that an amorphous layer deposited by molecular beam epitaxy annealed at or above 230 °C yields a textured-epitaxial structure among some randomly oriented domains. The textured-epitaxial Sb_2Se_3 grains are oriented with the covalent "1D axis" or [001] direction constrained in-plane to GaAs [110] and with multiple van der Waals (*hk*0) orientations out-of-plane. The same texture was achieved exclusively without randomly oriented grains using continuous-wave laser radiation, highlighting the use of thermal and optical methods to yield anisotropic crystalline Sb_2Se_3

films directly from the amorphous phase. Reflectance measurements and polarized microscopy confirm the unique state of in-plane birefringence in the crystallized thin film. Overall, we show that solid phase heteroepitaxy provides additional pathways to the integration of low-symmetry chalcogenide semiconductors for demanding applications where the inherent anisotropy needs to be preserved.

I. INTRODUCTION

Solid phase crystallization or solid phase epitaxy (SPE) is the process by which an amorphous solid phase transforms into an epitaxial crystalline phase due to templating influences from the substrate. While SPE has been most rigorously studied in the context of Si *homo*epitaxy for electronics,[1–3] more generally it has the potential to be an important synthesis route for optoelectronic and photonic device fabrication by *hetero*epitaxy. Such a method not only accesses a different regime of growth thermodynamics and kinetics,[4] but it also connects deeply to the operation of photonic phase change devices.

Solid-phase *hetero*epitaxy (hetero-SPE) holds exciting potential to integrate newer phase change materials (PCMs), such as Sb_2Se_3, which possesses lower orthorhombic *Pbnm* symmetry. Sb_2Se_3 has a near-infrared (near-IR) bandgap of 1.1-1.2 eV,[5–7] highly convenient for telecom band photonic applications.

Across the telecom bands, Sb_2Se_3 exhibits intrinsically lower loss compared to conventional PCM Ge-Sb-Te (GST) alloys that rely on complex compositional and bandgap engineering approaches.[8–12] Sb_2Se_3 further exhibits strongly direction-dependent absorption and refractive properties due its large bonding anisotropy — strong covalent

bonds exist along the [001] direction and weaker van der Waals (vdW) forces contribute to bonding along the other two directions, forming a quasi-1D structure.[13–18] Like other orthorhombic layered chalcogenides, including black phosphorus, SnSe, or GeSe, Sb_2Se_3 exhibits pronounced out-of-plane and in-plane anisotropy. Leveraging such direction-dependent thin film properties in semiconductors of lower crystallographic symmetry can enable advanced functionalities in optoelectronic and photonic devices.[19–23] Control over polarization and phase using birefringence underpins applications such as polarimetric photodetection and a range of beam modulation photonic devices including polarizers, rotators, and multiplexers.[24–30]

It remains challenging, however, to directly grow uniform thin films of birefringent materials such as Sb_2Se_3 on commercially relevant cubic or other high symmetry substrates. Often, the result is growth of multiple grain orientations or domains which average out the desired anisotropy in-plane. Poor orientation control also leads to lossy optical phase change devices. The scattering of light due to refractive index mismatch between randomly oriented grains was recently identified as the leading contributor to optical loss in Sb_2Se_3-based phase change devices.[31] Consequently, harnessing SPE to achieve epitaxial or textured grains of Sb_2Se_3 could enable new static photonic devices exploiting birefringence,[32] and simultaneously reduce scattering losses and increase index contrast in PCM devices.

Little precedent exists for using hetero-SPE to crystallize oriented thin films of anisotropic semiconductors. Vapor phase growth techniques commonly leverage substrate offcut or surface reconstructions that lower the symmetry of the starting template to successfully preserve orientation control in the film. This is convincingly shown in direct

vapor phase epitaxial growth of anisotropic semiconductors, including Sb_2Se_3. Most SPE studies, however, feature the classic isotropic semiconductors, such as Ge and III-V compounds on Si substrates,[4,33–36] in addition to GaN on sapphire substrates.[37] Among the few reports investigating amorphous-to-crystalline transformations of layered materials include hexagonal MoS_2. Although out-of-plane oriented regrowth was observed, it was not attributed to templating effects due to lack of an in-plane crystallographic relationship.[38,39]

As Sb_2Se_3 is conveniently deposited in the amorphous phase and has an accessible crystallization temperature around 200 °C,[40] our study clarifies how hetero-SPE may be a route to achieving oriented growth of orthorhombic Sb_2Se_3 directly onto commercially relevant cubic GaAs substrates. We perform thermal and laser heating crystallization experiments on a primary sample of a co-deposited amorphous Sb-Se film (~90 nm), from elemental Sb and Se cracker cells in a chalcogenide molecular beam epitaxy (MBE) chamber. No attempt was made to carefully control or measure the composition of the amorphous phase in the primary sample mentioned above, but additional samples with excess Se (noted only after crystallization) were also grown on GaAs and SiO_2 substrates. Structural characterization and optical birefringence in the primary film confirm that SPE, especially under laser heating, is a suitable method to achieve oriented growth of Sb_2Se_3 crystals.

II. EXPERIMENTAL

A. MBE growth of amorphous Sb-Se films

The native oxide of a commercial GaAs wafer was thermally desorbed in a III-V MBE system (Veeco Gen III) and roughly 100 nm of homoepitaxial GaAs was grown as a buffer layer. This substrate was then capped with amorphous arsenic before removal from the Gen III MBE and transferred into a separate IV-VI Riber Compact 21 (C21) MBE. In the Riber C21 chamber, the arsenic cap was thermally desorbed around a temperature of 420 °C. The substrate was then held to stabilize a (2×1) GaAs reconstruction, and finally the substrate was cooled to below 150 °C before growth. Temperatures were measured with optical pyrometry. No intentional selenium treatments were made to the GaAs surface prior to deposition, but the surface is likely selenium-stabilized due to the residual fluxes in the chamber. Co-deposited fluxes from valved Sb and Se cracker sources were used to grow the amorphous Sb-Se film directly on the homoepitaxial (2×1) GaAs surface. The beam equivalent pressures (BEPs) of Sb and Se were 5×10^{-8} Torr and 1×10^{-6} Torr, respectively.

B. Crystallization procedure

Samples were thermally crystallized in air (*ex situ*) using a FisherScientific hotplate. We intentionally did not deposit a protective encapsulation layer to prevent desorption as these layers may interfere with SPE by providing alternate nucleation sites.[41] To prevent severe oxidation, a silicon proximity wafer was kept above the film during the anneal.

Laser crystallization was performed using a 633 nm continuous-wave (CW) laser in a Horiba LabRAM HR Evolution instrument. The full laser power of 6.5 mW was reduced before incidence on the sample via neutral-density filters. The laser was focused

by an objective to achieve crystallized spots of approximately micron diameter. The dwell time was ranged from 1 s to 240 s. Crystallized patterns were written into the amorphous film by software-enabled stage movements.

A separate higher power 50 mW 532 nm CW laser was also used to produce crystallized spots of larger diameter. The sample was moved out of the focal plane to achieve defocused spot sizes at comparable power densities to the 633 nm laser.

C. Morphology characterization

Atomic force microscopy (AFM) scans were acquired on a Park NX10 instrument with a NCS15 probe in tapping mode. Scanning electron microscope (SEM) images were taken on a ThermoFisher Apreo (2 kV and 5 kV, 50 pA) using the Trinity T1 and T2 detectors.

D. Structural characterization

X-ray diffraction (XRD) scans were collected on a PANalytical Empyrean, using a parabolic mirror for the incident beam and parallel-plate collimator with a 2D solid-state hybrid PIXcel detector in 0D mode for the diffracted beam. The X-ray radiation source was Cu-Kα. 2D XRD patterns were collected using a Bruker D8 Venture single crystal diffractometer in a grazing incidence geometry with an Incoatec IμS microfocus Cu-Kα source and Photon 100 detector.

Raman spectra were collected on a Horiba LabRAM HR Evolution instrument with a 633 nm laser. A 600 gr/mm grating (7.2 cm^{-1} spectral resolution) was used for

thermally crystallized and power-dependent laser-crystallized films. A 300 gr/mm (13.3 cm^{-1} spectral resolution) was used for time-dependent laser-crystallized films. For the time-dependent series, the laser was rapidly scanned within a several microns area to simultaneously minimize heating and maximize signal, particularly aiding the collection of spectra acquired for 5 s.

E. Optical characterization

Optical anisotropy was probed with normal incidence reflectance versus beam polarization angle measurements, using a CW 532 nm laser. The linear polarization of the beam was adjusted via a half-wave plate set before the sample. The reflected signal was passed through a beamsplitter and collected by a ThorLabs CCD camera. The intensity of the reflected signal was quantified by integrating over the signal peak above a background threshold value and normalizing by the peak area.

Cross-polarized optical microscopy images in reflection mode were taken on a Nikon LV100 POL microscope with a rotation stage. The green channel images were used. The sample was placed and rotated between a crossed polarizer and analyzer to test for in-plane optical anisotropy.

III. RESULTS AND DISCUSSION

A. Crystallized microstructure and composition

We subjected a primary sample of amorphous Sb-Se to various thermal annealing and laser crystallization conditions and examined the resulting grain microstructure via atomic force microscopy (AFM) in **Figure 1**. Figures 1a-b show the as-grown structure

and the initially smooth film surface of RMS roughness 0.4 nm. The effect of increasing annealing temperature is first shown in Figures 1c-e, where all anneals were held for 120 s. At the lowest temperature of 210 °C, the film crystallizes into polycrystalline randomly oriented grains. Interestingly, as the temperature increases to 230 °C and 250 °C, the fraction of randomly oriented grains decreases whilst a second population of slightly elongated grains oriented along the horizontal direction emerges. These needle-like grains exhibit a long axis aligned to the [110] direction of the GaAs substrate and are ~500 nm to 1 μm in length. Such domains aligned to GaAs [110] may be textured or epitaxially aligned given their distinctly oriented morphology, to be discussed shortly in Figure 2.

The thermally annealed series suggests that higher temperatures promote growth of the needle-like Sb_2Se_3 grains, although not eliminating the fraction of randomly oriented grains. A further anneal performed at 270 °C produces a microstructure with a two grain population pattern similar to 250 °C (Figure S1), confirming that the fraction of aligned grains eventually plateaus with temperature. These findings suggest that temperature simultaneously increases the growth rate of randomly oriented crystallites[42] and the nucleation rates of aligned crystallites. This might lead to the observed situation where sufficiently fast growth of randomly oriented grains remains highly competitive with the nucleation and growth of the aligned grains.

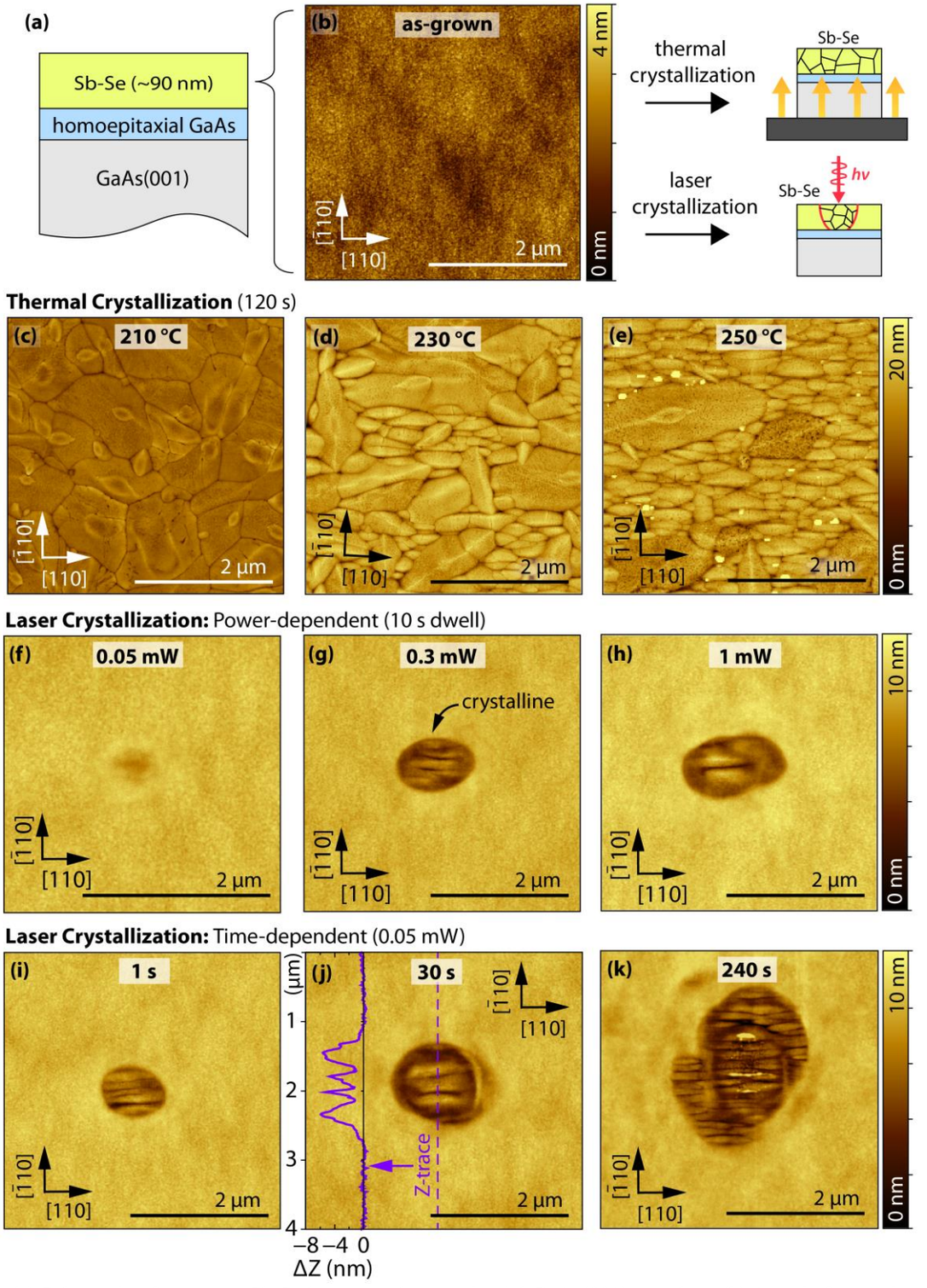

Figure 1. (a) Schematic of as-grown Sb-Se layer on a homoepitaxial GaAs(001) template. (b) Atomic force microscopy (AFM) scan of the as-grown Sb-Se film, which undergoes thermal and laser-induced crystallization. (c-e) AFM scan of Sb-Se after thermal annealing at 210 °C, 230 °C, and 250 °C, for 120 s. (f-h) AFM scans of laser-crystallized regions varying power at 0.05 mW (2-7 kW/cm^2), 0.3 mW (10-50 kW/cm^2), and 1 mW (60-200 kW/cm^2), with a 10 s dwell. (i-k) AFM images of laser-crystallized regions varying dwell time at 1 s, 30 s, and 240 s, using 0.05 mW (2-7 kW/cm^2). In (j), a representative Z-trace (height trace) through the crystallized spot shows the height change associated with crystalline transformation. The GaAs <110> directions are drawn for reference in all AFM images.

The RMS surface roughness increases from 0.4 nm in the as-grown film to 1.1 nm and 2.0 nm at 210 °C and 250 °C, respectively, and slight pitting of the grains occurs due to the high vapor pressure of Sb_2Se_3.[43] A final anneal at 300 °C was attempted but the film microstructural features are convoluted with the delamination of Sb_2Se_3. Additional scanning electron images and Raman spectroscopy of the films annealed at 270 °C and 300 °C reveal increased pitting and the onset of secondary oxide formation because of desorption (Figures S2-S3). Therefore, we use the film crystallized at 250 °C as the representative single phase, annealed film.

Next, we discuss spot crystallization induced by a stationary 633 nm laser upon varying power and dwell time parameters. A visible wavelength laser was chosen as it lies above the optical absorption edge for both amorphous Sb-Se (optical bandgap of 1.2 – 1.5 eV) and GaAs.[5,44–46] Power-dependent crystallization is shown in Figures 1f-h and time-dependent crystallization is shown in Figures 1i-k. We note that there is uncertainty on the power intensity (power per area), as we had explicit control over laser power but noted a range of focused spot sizes (spanning ~800 nm to 1.5 μm) between sets due to variance in optical alignment; we therefore express ranges of intensity. We find the relative progression of crystallization is reproducible within the individual sets, but we did not make absolute comparisons between the sets to account for the uncertainty.

In the power-dependent series, Figure 1f indicates that a crystallization threshold achieved at 0.05 mW (2-7 kW/cm^2) must be exceeded to induce structural transformation. Near this threshold power density, a partial cavity forms at the laser focus point. Higher intensities produce larger cavities which eventually expose the interior of the crystallized spots. We observe grains of a distinct needle-like morphology oriented along the GaAs

[110] direction, similar to the majority fraction in the 250 °C annealed film. The local depression in height of the laser-irradiated spots are due to densification in the crystalline phase and potentially some material evaporation.

Longer dwell times were also found to increase the radius of crystallization. In Figures 1i-k, the dwell time was varied from 1 s to 240 s at 0.05 mW (2-7 kW/cm^2). A representative height profile has been traced through the spot generated under a 30 s dwell time, which captures: 1) the several nanometers height change at the amorphous-crystalline boundary and 2) the needle-like morphology within the crystalline region interior.

We also rule out the role of laser polarization in setting the morphology and demonstrate crystallization with a 532 nm laser (supplementary material, Section B). The absorption coefficients of Sb_2Se_3 at 633 nm and 532 nm both exceed 10^5 cm^{-1},[6,11,12] implying near-complete absorption of both wavelengths and similar temperature gradients are expected across the film. Overall, these results point to the in-plane oriented Sb_2Se_3 morphology being a reproducible phenomenon under accessible power densities and multiple visible wavelengths.

An apparent difference between thermal annealing and laser crystallization is that the latter method circumvents randomly oriented growth and consists exclusively of elongated grains oriented to GaAs [110], suggesting different heating methods offer control in the competition between random vs oriented growth.[4] The uniform microstructure was verified in additional laser-crystallized spots up to 100 μm diameter (Figure S4). It is possible that in the thermally annealed films, the randomly oriented

grains have stochastically nucleated within the bulk of the film, as opposed to at the film-substrate interface where the templating influence is strongest.

We speculate that the laser-induced heat profile and transience yield a gradient of temperatures within the film that strongly favor film-substrate interface nucleation events crucial to SPE.[47] The crystallization mechanism upon CW irradiation in this work is likely photothermal, involving processes such as carrier thermalization, non-radiative recombination, and longer timescale thermal diffusion.[48] We estimate steady-state carrier concentrations up to ~10^{17}-10^{18} cm^{-3} are achieved under our illumination conditions, which fall much below the power intensities necessary to induce electronic (athermal) effects in structural transformations of phase change materials such as GST.[49]

We show X-ray diffraction (XRD) in **Figure 2** to resolve the crystallographic orientation of Sb_2Se_3 grains oriented along GaAs [110]. We follow the *Pbnm* convention to index Sb_2Se_3. The symmetric out-of-plane scans in Figure 2a exhibit no sharp peaks for the as-grown amorphous film while several reflections from multiple (*hk*0)-planes of Sb_2Se_3 are visible after the 250 °C thermal anneal. The (*hk*0) indices indicate that the covalently bonded [001] axis lies in-plane. From our observations of an oriented grain morphology, the [001] axis is further constrained along the GaAs [110] direction by the underlying template. However, the film is not single domain as the grains have discrete rotations about the [001] axis, as schematically illustrated in Figure 2b. This microstructure, termed "(*hk*0)-oriented", is therefore multi-crystalline with strongly textured-epitaxial alignment. We note that this structure was similarly identified in prior work on direct vapor phase growth of Sb_2Se_3 films on GaAs by MBE.[50] An out-of-plane

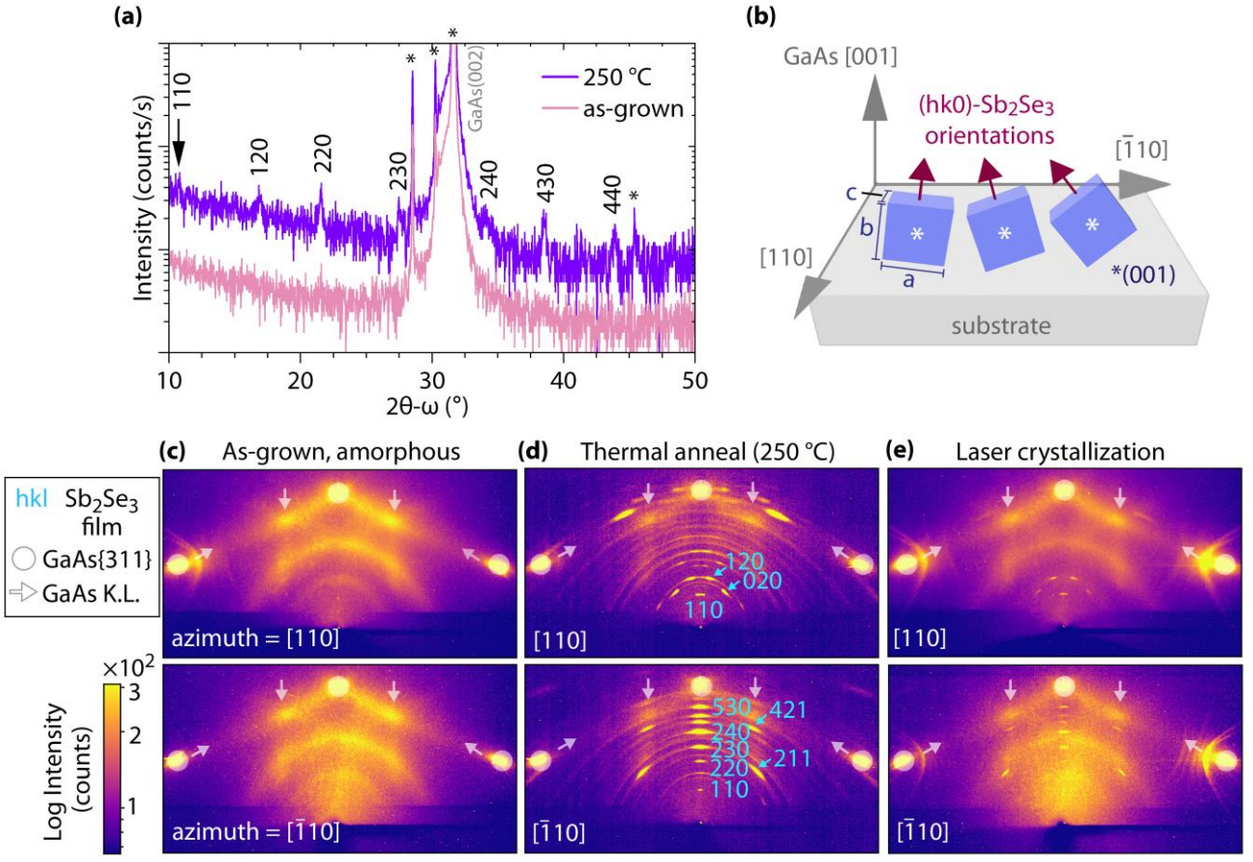

Figure 2. (a) X-ray diffraction out-of-plane scans of 250 °C thermally annealed film and as-grown Sb-Se reference film. GaAs substrate peaks including related spectral reflections and artifacts are labeled with an asterisk. The scans are vertically offset for clarity. (b) Schematic of Sb_2Se_3 orthorhombic unit cells with (*hk*0) orientations out-of-plane and the (001) normal aligned to GaAs [110] in-plane. (c-e) GIXS diffraction patterns collected along the GaAs [110] and [1̄10] azimuths of as-grown amorphous film, 250 °C thermally annealed film, and (e) laser-crystallized domain (~100 µm). Crystallized Sb_2Se_3 Bragg reflections (*hkl*) are highlighted in cyan, and substrate reflections and Kikuchi lines (K.L.) in white.

scan on the more ordered microstructure of the laser-crystallized spot was not possible due to insufficient diffraction volume.

To overcome this limitation, we collected diffraction patterns (DPs) via grazing incidence scattering (GIXS) at 5° incidence angle with a reduced X-ray spot size. The micro-focused probe was positioned on an isolated ~100 µm laser-crystallized spot (from Figure S2), with the beam footprint approaching 1 mm at the shallow incidence angle. The DPs imaged with the incident wavevector along the distinct GaAs [110] and [-110]

azimuths are shown in Figures 2c-e for the pristine amorphous phase, 250 °C annealed, and laser-crystallized structures, respectively.

As expected, the amorphous Sb-Se phase shows diffuse scattering independent of the sample azimuth (Figure 2c). In Figure 2d, the thermally crystallized film pattern exhibits a complex combination of randomly oriented polycrystalline and textured-epitaxial structures, seen by the superimposed Debye Scherrer rings (indexed in Figure S5) and the higher intensity ordered reciprocal lattice (RL) points. The ordered RL points are indexed in blue. The Sb_2Se_3 film indeed displays a two-fold symmetry in-plane since the ordered RL points change between the GaAs [110] and $[\bar{1}10]$ azimuth. The reflection indices in the GaAs [110] DP also confirm this direction is approximately along the [001] zone of Sb_2Se_3. The diffraction rings and spots, in addition to the film mosaicity, are discussed in further detail in supplementary material, Section C.

In Figure 2e, we present the laser-crystallized DP which is composed of ordered diffraction spots from the isolated crystalline region and diffuse scattering from the surrounding amorphous matrix. Importantly, the diffraction spots generated by laser-crystallized Sb_2Se_3 appear at identical positions to those in the thermally crystallized DP. This confirms that the ordered laser- and thermally-crystallized Sb_2Se_3 grains grow with the [001] axis aligned along GaAs [110] in-plane and exhibit mixed (*hk*0)-orientations normal to the substrate. The [001] axis is befittingly termed the "1D axis" or "needle axis" because the crystals can form with significant aspect ratios. Overall, these results validate the hypothesis that lower substrate surface symmetry can bias SPE for anisotropic film growth of Sb_2Se_3 on GaAs, even though the GaAs bulk has a higher cubic symmetry.

Raman spectra shown in **Figure 3** confirm a transformation from an amorphous state to the orthorhombic phase in the primary sample. Laser crystallization of the pristine material happens in parallel with Raman signal acquisition, so the laser power or integration (dwell) time may be treated as a proxy for the extent of crystallization. Within the laser power-dependent series, a weak signature of the amorphous phase is initially observed at 0.05 mW (2-7 kW/cm^2). The spectra evolves to exhibit increasingly sharper crystalline modes, especially near the 191 cm^{-1} Sb-Se bond vibration frequency,[51] at 0.15 mW (7-20 kW/cm^2) and 0.3 mW (10-50 kW/cm^2). (The 191 cm^{-1} mode is one of the primary modes assigned to the orthorhombic Sb_2Se_3 phase.[52]) The time-dependent crystallization series performed at 0.05 mW (2-7 kW/cm^2) similarly shows an increasing progression in crystallinity from 5 s to 30 s.

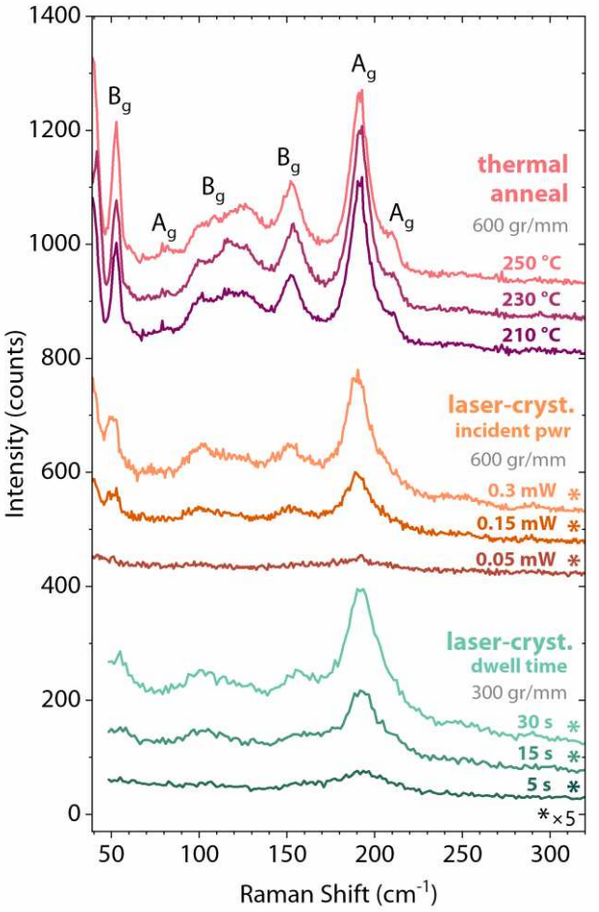

Figure 3. Raman spectra of thermally annealed, 633 nm laser-crystallized power-dependent, and laser-crystallized time-dependent series. The thermally annealed spectra are integrated across 300 s; power-dependent measurements are integrated across 10 s, and time-dependent measurements are performed at 0.05 mW (2-7 kW/cm^2). All laser-crystallized spectra have been scaled by 5×.

Comparison of the power-dependent and time-dependent series Raman modes to those of the 210-250 °C thermally annealed films confirms that both laser crystallization and thermal annealing yield the orthorhombic Sb_2Se_3 phase. The thermally annealed series exhibits the main modes of Sb_2Se_3: at 191 cm^{-1} (A_g), the shoulder on the blue side around 210 cm^{-1} (A_g), and 153 cm^{-1} (B_g).[52] We also see a broad central 100 cm^{-1} to 140 cm^{-1} region which consists of several overlapping low intensity modes. Modes in this region have tentative B_g symmetry assignments,[52,53] and are not well resolved by 633 nm excitation (as is observed also in single crystal Sb_2Se_3).[52] We further note two sharp

modes in the low frequency region at 53 cm^{-1} and ~39 cm^{-1}. These low frequency modes are not commonly captured due to filter cutoff limitations, but were reported recently for the first time by Kumar *et al*.[54]

Stoichiometry regulation is important to phase change devices, as large non-stoichiometric tolerances in the amorphous phase can eventually contribute to composition-related failure. A chalcogen-deficient material produces incomplete crystallization whereas a chalcogen-excess material becomes phase separated; both lead to inconsistent cycling and premature drifts in optical properties if atomic migration processes or composition gradients form.

Importantly, we do not see scattering from secondary phases in our spectra after crystallization, notably excess elemental Sb or Se which vibrate most intensely at 155 cm^{-1} and 240 cm^{-1} to 255 cm^{-1}, respectively.[55–59] This suggests a near-stoichiometric starting composition of the amorphous phase in our primary sample that is close to Sb_2Se_3, possibly achieved due to warm conditions in the MBE chamber and our flux ratios which regulated excess Se sticking. Although our Raman spectra suggest that we have synthesized a near-stoichiometric amorphous phase, it is unlikely that quenched films are, in general, near-stoichiometric. We briefly test the effect of deviating from this composition towards the chalcogen-rich side on the outcomes of crystallization.

A 250 °C thermal anneal was performed on an intentionally selenium-rich film on GaAs and on an additional SiO_2 control substrate. AFM and SEM images comparing the crystallized morphology are shown in Figure S7, alongside XRD measurements in Figures S8-S10. We find that in-plane oriented growth of Sb_2Se_3 still occurs on GaAs but is punctuated by non-contacting grain boundaries likely due to segregation and then

evaporation of excess Se.[60] Interestingly, the [100] orientation becomes most favorable, indicating that the amount of Se stabilizes different preferred orientations. The film crystallized on SiO_2 shows similar discontinuities in the film related to Se evaporation but exhibits completely random orientations (verified by the GIXS pattern in Figure S8c) due to the amorphous SiO_2 template. Raman measurements in Figure S9 confirm the presence of excess Se in both films on GaAs and SiO_2. Further work is needed to correlate the Se content to interfacial energies and thus the resulting primary orientation(s) in recrystallized films prepared on GaAs and other substrates.

B. Optical anisotropy

The mixed (*hk*0)-oriented crystallized regions in our primary sample exhibit in-plane anisotropy in the form of birefringence. In-plane birefringence should arise even in our non-single domain oriented films as the Sb_2Se_3 orthorhombic crystal has three distinct optical indices due to differences in bond polarizability. The covalently bonded [001] direction that is the most polarizable, hence highest index, is aligned to GaAs [110]. A combination of the [-*kh*0] weaker vdW bonded directions, hence lower index, lies perpendicular along the GaAs [-110] direction.

We demonstrate this optical anisotropy at 532 nm via normal incidence reflectance measurements vs incident polarization angle. In **Figure 4**, the normalized reflectance of the as-grown amorphous film is compared to the same film after 250 °C thermal annealing and laser crystallization. The polarization angle of the laser is defined with reference to the vertical in-plane direction of GaAs [-110] for consistency.

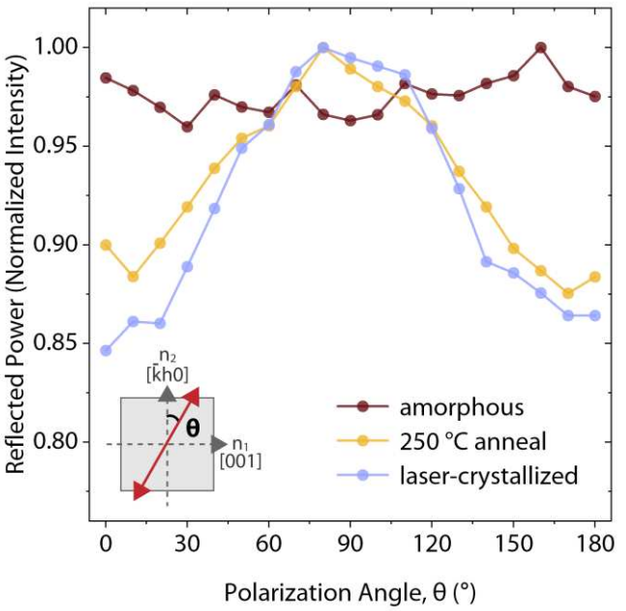

Figure 4. Normalized reflected power (532 nm) versus polarization angle, θ, for the Sb-Se film in the as-grown amorphous condition, after 250 °C annealing, and after 532 nm laser crystallization. In-plane indices of crystalline Sb_2Se_3, n_1 [001] and n_2 [-kh0], correspond to the needle axis and vdW directions, respectively.

In Figure 4, the reflectance of the isotropic amorphous phase remains relatively constant when rotating the beam polarization, whereas the reflectance of the annealed and laser-crystallized film exhibits a two-fold pattern or 180° period. The beam polarization is initially parallel to a combination of [-kh0] directions in Sb_2Se_3. The reflectance increases as the incident polarization becomes parallel to the [001] direction or needle axis at 90°. An angular dependence in the reflectance indicates that an isotropic-to-anisotropic optical response is concurrent with the amorphous-to-epitaxial structural transformation.

The relative change or modulation in reflectance of crystallized Sb_2Se_3 at 532 nm are approximately 11% and 14% for the annealed and laser-crystallized case, respectively. The magnitude of modulation between the two in-plane crystal axes for the laser-crystallized film (14%) is close to a predicted estimate of 15% derived from the

Fresnel equations (refer to calculations in supplementary material, Section E). The lower reflectance modulation observed in the thermally annealed film (11%) may be attributed to the randomly oriented grains distributed throughout the crystallized volume. We identified previously in Figure 1 that the thermally annealed films contain a minority fraction of randomly oriented Sb_2Se_3 grains, although far from a negligible quantity.

We next subject the samples to polarized optical microscopy (POM) to assess the spatial extent of birefringent domains within the complex microstructure in **Figure 5**. The GaAs [110] direction was manually aligned to the horizontal, which subsequently aligns the two in-plane refractive indices of Sb_2Se_3 to the perpendicular 0° and 90° positions in the microscope frame of reference. With the polarizer and analyzer crossed at the 0°/90° positions, we present the (brightness-contrast adjusted) green channel images of the white light reflection upon sample rotation.

Briefly, strong birefringence, dichroism, or both in anisotropic crystals can result in 90°-periodic bright POM images. The dimmest intensities are observed when the crystal orientation meets special extinction conditions where the incident polarization falls parallel to a principal index direction (at 0° and 90° for orthorhombic crystal axes); the reflected beam maintains the same polarization state and is therefore blocked by the analyzer. Cross-polarized (CP) imaging is exceptionally sensitive to optical anisotropy, as intensity may only be projected onto the analyzer if the sample induces elliptical polarization, through reflection amplitude or phase differences between the orthogonally polarized reflected beams. The projected intensity becomes brightest near diagonal rotation angles of 45° or 135°.[61]

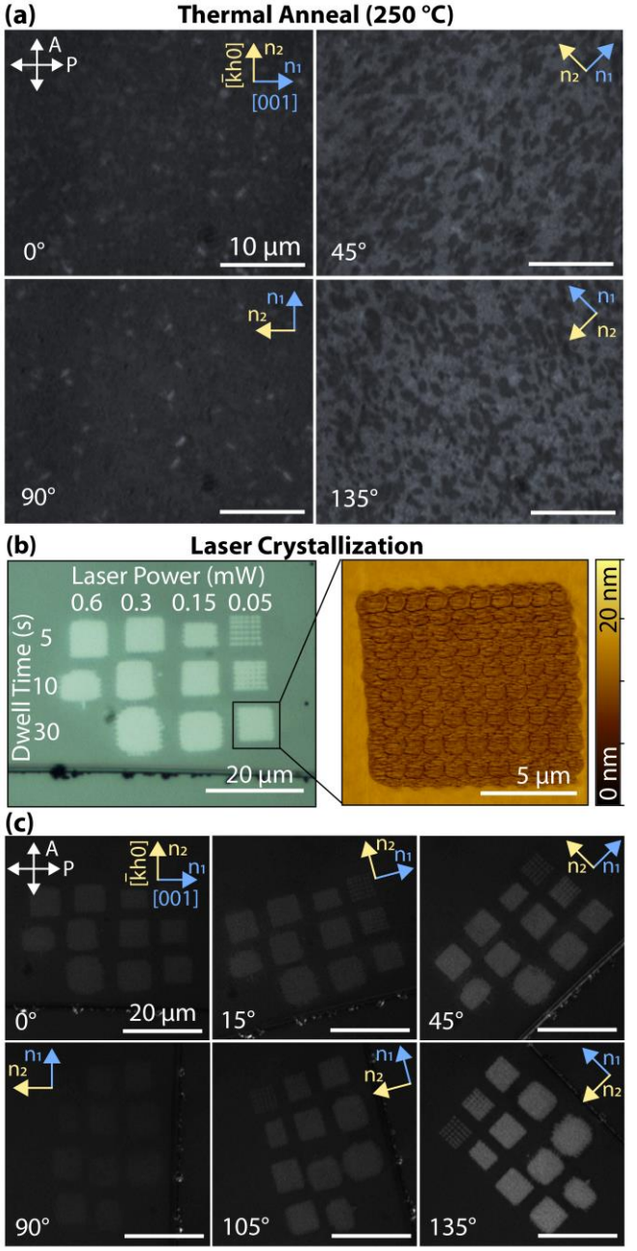

Figure 5. Polarized optical imaging (POM) of 250 °C thermally annealed and laser-crystallized films to reveal in-plane optical anisotropy. (a) POM of 250 °C annealed Sb-Se film at rotation angles of 0°, 45°, 90°, and 135°. The aligned Sb_2Se_3 majority fraction has two in-plane indices, n_1 [001] and n_2 [-kh0], which correspond to the needle axis and vdW directions, respectively. (b) Unpolarized optical image of laser-crystallized pattern under conditions of 0.05-0.6 mW and dwell times of 5-30 s, including an atomic force microscopy scan of a fully crystallized domain. (c) POM of the laser-patterned film in (b) at several rotation angles. In-plane indices of Sb_2Se_3, n_1 [001] and n_2 [-kh0], correspond to the needle axis and vdW directions, respectively.

In Figure 5a, the thermally annealed sample is shown to be mostly dark at 0° and 90°, reflecting the majority fraction of grains which have distinct optical indices parallel

to the 0°/90° positions. The 0° and 90° images are flecked with several bright grains, which are misaligned grains and consistent with our observations of randomly oriented grains present in the film. Upon rotation to intermediate angles of 45° and 135°, the overall intensity brightens, highlighting a mottled microstructural contrast. The brighter regions correspond to the aligned (*hk*0)-oriented grains within the film and likewise, the darker patches arise from the misoriented grains.

We have additionally laser-crystallized patches of the pristine amorphous film using various dwell times and power densities to embed a square-based pattern. As shown in Figure 5b under unpolarized imaging, the brighter crystalline regions appear distinctly against the darker background of the amorphous film due to different optical constants. AFM confirms that the entirety of the bright region is comprised of aligned grains. All anisotropic crystalline domains are then easily distinguished from the isotropic amorphous matrix by rotating the sample in Figure 5c — only the intensity of the crystalline area increases, whereas the amorphous (isotropic) background remains dark. Unlike the thermally crystallized film, the laser-crystallized regions do not contain various randomly oriented grains, and thus the optical contrast is observed to be quite uniform at 45°/135°.

In the thermally annealed film, the randomly oriented aligned grains occupy a volume fraction of roughly 30%, sufficient to reduce the maximum reflectance modulation from 14% to 11% (previously noted in Figure 4). Additional impacts to device performance, such as the grain boundary scattering losses generated by this bimodal grain population, could be investigated in future work.

Overall, the POM images indeed demonstrate periodic extinction (a signature of anisotropic crystals) but the contrast at 45° is dim. This falls under our expectations for crystalline Sb_2Se_3, where the combined effects of strong birefringence and dichroism in the visible wavelengths govern the resulting image intensities. At a wavelength of 532 nm, for example, we estimate a miniscule (close to zero) phase difference is accumulated between the two reflected orthogonal beams polarized along GaAs [110] and [-110], such that the reflected light is nearly linearly-polarized (supplementary material, Section E). The different reflection amplitudes are then largely responsible for generating the observed intensity through the analyzer. At an incident polarization of 45°, the different reflection amplitudes rotate the reflected light by only ~2°. The situation here is an extremely narrow polarization ellipse exhibiting slight overlap with the analyzer. Nevertheless, this still generates sufficient signal under CP to spatially distinguish anisotropic from isotropic domains in our films.

C. Interpretation of substrate effects

We have shown that the GaAs template orders the crystallization of Sb_2Se_3 films yielding in-plane anisotropy, although not yielding a single crystal domain. We now discuss why the grains preferentially align their [001] or needle axis to GaAs [110]. VdW materials typically facet along the layered direction to minimize interfacial energy, resulting in covalently bonded layers parallel to the substrate. It is plausible that layered quasi-1D materials like Sb_2Se_3 exhibit similar tendencies. If surface energies of several planes perpendicular to the covalent 1D axis are comparable,[62] multiple orientations could be low energy accessible while still maintaining the covalent axis in-plane. Laser

and thermal crystallization of isostructural stibnite (Sb_2S_3) on glass also demonstrated preference of the [001] axis to lie in-plane, but the crystals were not constrained to a particular in-plane direction.[63,64]

Alternate mechanisms beyond surface energy minimization have been proposed to drive in-plane [001] growth of Sb_2S_3 in glass, including potential sensitivity of the [001] direction to laser polarization or asymmetric thermal profile of the beam.[63] In our work, Sb_2Se_3 remains aligned to GaAs under stationary beam conditions and is not affected by beam polarization, implying that an anisotropic templating influence must be central to setting the [001] direction. We first examine the lattice mismatch between orthorhombic Sb_2Se_3 (a = 11.63 Å, b = 11.78 Å, c = 3.98 Å) and GaAs (a = 5.65 Å). Tensile mismatches of 3% and 1.8% exist between the a- and b-directions to GaAs [110], respectively, using a d_{SbSe} : $3d_{GaAs}(110)$ ratio. The c-direction exhibits a smaller and more favorable 0.5% mismatch to GaAs [110], using $d_{SbSe}(001)$: $d_{GaAs}(110)$. However, it was demonstrated that as-grown crystalline Sb_2Se_3 films also grew with the needle axis along the [110] direction of other cubic templates, such as PbSe (a = 6.12 Å) with a much more severe mismatch of 8%.[50] As the lattice mismatch criterion is substantially relaxed for vdW materials,[65] this points to other interface characteristics not entirely encapsulated by lattice mismatch, such as anisotropic surface diffusion, that might encourage preferential growth of Sb_2Se_3 along the [110] cubic diagonal.

We know from homo-SPE studies on Si that the interface structure has appreciable influence on the reordering of the first several atomic layers.[66] We have no evidence that the initial (2×1) GaAs selenium-stabilized surface reconstruction persists under the amorphous film to template the crystallization; the reconstruction may be

buried, of an altered symmetry, or otherwise ill defined. We assume simply and refer to the anisotropic structure of the unreconstructed (001) zincblende surface. Substrate effects extending several layers deeper than the uppermost surface layer can affect the film. In zincblende crystals, the second layer of atoms beneath the surface layer exhibits a non-equivalent atomic arrangement between [110] and the orthogonal [-110] direction,[67,68] perhaps allowing the substrate to bias in-plane diffusion and crystallization of Sb_2Se_3.

IV. SUMMARY AND CONCLUSIONS

We have demonstrated that the Sb_2Se_3 recrystallization orientation is preferential on a GaAs(001) template, yielding anisotropic orthorhombic grains in- and out-of-plane. Crystallization was achieved using facile heating methods of thermal annealing and the action of a 633 nm and 532 nm laser. Above a 230 °C annealing temperature, there is a partial fraction of Sb_2Se_3 grains with the [001] needle axis aligned to GaAs [110] and mixed (*hk*0) orientations out-of-plane. Laser-crystallized domains share the same structure. Furthermore, laser-crystallized domains show a complete fraction of aligned grains, suggesting further optimization of different heating methods and related parameters can achieve uniformly patterned anisotropic Sb_2Se_3 crystals potentially with a variety of microheater, electron, or ion beam mechanisms.

We confirm that a technologically a technologically useful and rare property of in-plane birefringence is realized in crystallized Sb_2Se_3 films. The crystallographic alignment implies that out-of-plane birefringence must be necessarily present, consistent with the orthorhombic symmetry of Sb_2Se_3. This distinguishes biaxial orthorhombic thin

films from uniaxial tetragonal or hexagonal films, which commonly exhibit out-of-plane anisotropy in the *c*-axis orientation, but remain isotropic within the basal or substrate plane.

The role of solid-phase epitaxy as a pathway between an amorphous (isotropic) to epitaxial (anisotropic) state opens further investigation, particularly in the context of cycling optical phase change devices. Studies on the reversibility of this transition and the feasibility of achieving single crystals via SPE would benefit applications that harness directionality or birefringence in the crystalline phase, integrating native and tunable polarization-sensitive interactions into conventional thin films.

SUPPLEMENTARY MATERIAL

The supplementary material contains: AFM, SEM, and Raman spectroscopy of thermally annealed films; AFM of additional laser-crystallized spot; GIXS analysis of thermally annealed and laser-crystallized film; AFM, SEM, XRD/GIXS, and Raman spectroscopy comparison of selenium-excess films on GaAs and SiO_2 substrates; reflectance estimation calculations.

ACKNOWLEDGMENTS

We gratefully acknowledge support via the NSF CAREER award under Grant No. DMR-2036520. Part of this work was performed at the Stanford Nanofabrication Facilities (SNF) and Stanford Nano Shared Facilities (SNSF), supported by the National Science

Foundation under award ECCS-2026822. A.M.L. and Y.S. acknowledge support from the Department of Energy, Office of Basic Energy Sciences, Division of Materials Sciences and Engineering, under contract DE-AC02-76SF00515.

AUTHOR DECLARATIONS

Conflicts of Interest

The authors have no conflicts to disclose.

DATA AVAILABILITY

The data that supports the findings of this study are available within the article and its supplementary material.

REFERENCES

[1] J.W. Mayer, L. Eriksson, S.T. Picraux, and J.A. Davies, Can. J. Phys. **46**(6), 663–673 (1968).
[2] G.L. Olson, and J.A. Roth, Mater. Sci. Rep. **3**(1), 1–77 (1988).
[3] F. Priolo, and E. Rimini, Mater. Sci. Rep. **5**(6), 319–379 (1990).
[4] M.A. Herman, W. Richter, and H. Sitter, *Epitaxy: Physical Principles and Technical Implementation* (Springer, Berlin, Heidelberg, 2004).
[5] P. Singh, N. Ghorai, A. Thakur, and H.N. Ghosh, J. Phys. Chem. C **125**(9), 5197–5206 (2021).
[6] C. Chen, W. Li, Y. Zhou, C. Chen, M. Luo, X. Liu, K. Zeng, B. Yang, C. Zhang, J. Han, and J. Tang, Appl. Phys. Lett. **107**(4), 043905 (2015).
[7] F. Kosek, J. Tulka, and L. Štourač, Czech. J. Phys. **28**(3), 325–330 (1978).
[8] Y. Zhang, J.B. Chou, J. Li, H. Li, Q. Du, A. Yadav, S. Zhou, M.Y. Shalaginov, Z. Fang, H. Zhong, C. Roberts, P. Robinson, B. Bohlin, C. Ríos, H. Lin, M. Kang, T. Gu, J. Warner, V. Liberman, K. Richardson, and J. Hu, Nat. Commun. **10**(1), 4279 (2019).
[9] C. Koch, A.-L. Hansen, T. Dankwort, G. Schienke, M. Paulsen, D. Meyer, M. Wimmer, M. Wuttig, L. Kienle, and W. Bensch, RSC Adv. **7**(28), 17164–17172 (2017).
[10] E.M. Vinod, K. Ramesh, and K.S. Sangunni, Sci. Rep. **5**(1), 8050 (2015).
[11] K. Aryana, H.J. Kim, Md.R. Islam, N. Hong, C.-C. Popescu, S. Makarem, T. Gu, J. Hu, and P.E. Hopkins, Opt. Mater. Express **13**(11), 3277 (2023).

[12] M. Delaney, I. Zeimpekis, D. Lawson, D.W. Hewak, and O.L. Muskens, Adv. Funct. Mater. **30**(36), 2002447 (2020).
[13] J. Black, E.M. Conwbll, L. Seigle, and C.W. Spencer, J. Phys. Chem. Solids **2**(3), 240–251 (1957).
[14] M. Schubert, T. Hofmann, C.M. Herzinger, and W. Dollase, Thin Solid Films **455–456**, 619–623 (2004).
[15] G.P. Voutsas, A.G. Papazoglou, P.J. Rentzeperis, and D. Siapkas, Z. Kristallogr. - Cryst. Mater. **171**, 261–268 (1985).
[16] S. Šćavničar, Z. Kristallogr. **114**, 85–97 (1960).
[17] S. Niu, G. Joe, H. Zhao, Y. Zhou, T. Orvis, H. Huyan, J. Salman, K. Mahalingam, B. Urwin, J. Wu, Y. Liu, T.E. Tiwald, S.B. Cronin, B.M. Howe, M. Mecklenburg, R. Haiges, D.J. Singh, H. Wang, M.A. Kats, and J. Ravichandran, Nat. Photon. **12**(7), 392–396 (2018).
[18] B. Zhao, H. Mei, Z. Du, S. Singh, T. Chang, J. Li, B. Ilyas, Q. Song, T. Liu, Y. Shao, R. Comin, N. Gedik, N.S. Settineri, S.J. Teat, Y. Chen, S.B. Cronin, M.A. Kats, and J. Ravichandran, Adv. Opt. Mater. **12**(29), 2400327 (2024).
[19] X. Li, H. Liu, C. Ke, W. Tang, M. Liu, F. Huang, Y. Wu, Z. Wu, and J. Kang, Laser Photonics Rev. **15**(12), 2100322 (2021).
[20] Y. Zhang, J. Wu, L. Jia, D. Jin, B. Jia, X. Hu, D. Moss, and Q. Gong, Npj Nanophoton. **1**(1), 28 (2024).
[21] Z. Lin, X. Yang, J. He, N. Dong, and B. Li, Appl. Phys. Rev. **12**(1), 011301 (2025).
[22] Z. Li, B. Xu, D. Liang, and A. Pan, Research **2020**, 2020/5464258 (2020).
[23] A. Singh, S.S. Jo, Y. Li, C. Wu, M. Li, and R. Jaramillo, ACS Photonics **7**(12), 3270–3285 (2020).
[24] Y. Han, and G. Li, Opt. Express **13**(19), 7527 (2005).
[25] H. Yuan, X. Liu, F. Afshinmanesh, W. Li, G. Xu, J. Sun, B. Lian, A.G. Curto, G. Ye, Y. Hikita, Z. Shen, S.-C. Zhang, X. Chen, M. Brongersma, H.Y. Hwang, and Y. Cui, Nat. Nanotechnol. **10**(8), 707–713 (2015).
[26] S. Li, J. Zhang, L. Zhu, K. Zhang, W. Gao, J. Li, and N. Huo, Adv. Funct. Mater. **33**(11), 2210268 (2023).
[27] F. Xia, H. Wang, and Y. Jia, Nat. Commun. **5**(1), 4458 (2014).
[28] M. Yuan, X. Han, H. Xiao, T.G. Nguyen, A. Boes, G. Ren, Q. Hao, J. Xue, A. Mitchell, and Y. Tian, Opt. Lett. **48**(1), 171 (2023).
[29] Z. Lin, Y. Lin, H. Li, M. Xu, M. He, W. Ke, H. Tan, Y. Han, Z. Li, D. Wang, X.S. Yao, S. Fu, S. Yu, and X. Cai, Light Sci. Appl. **11**(1), 93 (2022).
[30] S. Zhang, H. Wang, M.M. Kirchner, J. Liu, H. Luo, Y. Ren, C. Yuan, H.T. Hattori, A.E. Miroshnichenko, and W. Lei, Adv. Mater. Interfaces **9**(17), 2200448 (2022).
[31] J. Li, Y. Yun, K. Xu, J. Zhang, H. Lin, Y. Zhang, J. Hu, and T. Gu, IEEE J. Sel. Top. Quantum Electron. **30**(4), 1–9 (2024).
[32] G.Y. Jung, G. Ren, P. Omprakash, J. Ravichandran, and R. Mishra, Chem. Mater. **37**(15), 5796–5804 (2025).
[33] K.I. Cho, W.K. Choo, S.C. Park, T. Nishinaga, and B.-T. Lee, Appl. Phys. Lett. **56**(5), 448–450 (1990).
[34] K. Yoshino, K. Murakami, S. Yokoyama, and K. Masuda, Appl. Phys. Lett. **54**(25), 2562–2564 (1989).

[35] I. Suzumura, M. Okada, A. Muto, Y. Torige, H. Ikeda, A. Sakai, S. Zaima, and Y. Yasuda, Thin Solid Films **369**(1–2), 116–120 (2000).
[36] R.R. Lieten, S. Degroote, M. Leys, N.E. Posthuma, and G. Borghs, Appl. Phys. Lett. **94**(11), 112113 (2009).
[37] N. Ohshima, H. Yonezu, S. Yamahira, and K. Pak, J. Cryst. Growth **189–190**, 275–281 (1998).
[38] M. Krbal, J. Prikryl, V. Prokop, I. Pis, F. Bondino, and A.V. Kolobov, Appl. Phys. Lett. **121**(19), (2022).
[39] L. Fei, S. Lei, W.-B. Zhang, W. Lu, Z. Lin, C.H. Lam, Y. Chai, and Y. Wang, Nat. Commun. **7**(1), 12206 (2016).
[40] E. Černošková, R. Todorov, Z. Černošek, J. Holubová, and L. Beneš, J. Therm. Anal. Calorim. **118**(1), 105–110 (2014).
[41] T.Y. Teo, N. Li, L.Y.M. Tobing, A.S.K. Tong, D.K.T. Ng, Z. Ren, C. Lee, L.Y.T. Lee, and R.E. Simpson, ACS Photonics **10**(9), 3203–3214 (2023).
[42] F. Hoff, J. Pries, J. Köttgen, P. Lucas, and M. Wuttig, Adv. Phys. Res. **4**(9), 2500005 (2025).
[43] V. Piacente, P. Scardala, and D. Ferro, J. Mater. Sci. Lett. **11**(12), 855–857 (1992).
[44] M.D. Sturge, Phys. Rev. **127**(3), 768–773 (1962).
[45] R. Mueller, and C. Wood, J. Non-Cryst. Solids **7**(4), 301–308 (1972).
[46] P. Arun, and A.G. Vedeshwar, Thin Solid Films **335**(1–2), 270–278 (1998).
[47] S.A. Kokorowski, G.L. Olson, and L.D. Hess, J. Appl. Phys. **53**(2), 921–926 (1982).
[48] S.K. Sundaram, and E. Mazur, Nature Mater **1**(4), 217–224 (2002).
[49] P. Fons, P. Rodenbach, K.V. Mitrofanov, A.V. Kolobov, J. Tominaga, R. Shayduk, A. Giussani, R. Calarco, M. Hanke, H. Riechert, R.E. Simpson, and M. Hase, Phys. Rev. B **90**(9), 094305 (2014).
[50] K. Xiao, V. Tara, P.D. Reddy, J.E. Meyer, A.M. Skipper, R. Chen, L.J. Nordin, A. Majumdar, and K. Mukherjee, Mater. Horiz., **12**, 5829–5838 (2025).
[51] J. Ibáñez, J.A. Sans, C. Popescu, J. López-Vidrier, J.J. Elvira-Betanzos, V.P. Cuenca-Gotor, O. Gomis, F.J. Manjón, P. Rodríguez-Hernández, and A. Muñoz, J. Phys. Chem. C **120**(19), 10547–10558 (2016).
[52] P. Vidal-Fuentes, M. Guc, X. Alcobe, T. Jawhari, M. Placidi, A. Pérez-Rodríguez, E. Saucedo, and V.I. Roca, 2D Mater. **6**(4), 045054 (2019).
[53] N. Fleck, T.D.C. Hobson, C.N. Savory, J. Buckeridge, T.D. Veal, M.R. Correia, D.O. Scanlon, K. Durose, and F. Jäckel, J. Mater. Chem. A **8**(17), 8337–8344 (2020).
[54] A. Kumar, V. Kumar, A. Romeo, C. Wiemer, and G. Mariotto, J. Phys. Chem. C **125**(36), 19858–19865 (2021).
[55] A.H. Goldan, C. Li, S.J. Pennycook, J. Schneider, A. Blom, and W. Zhao, J. Appl. Phys. **120**(13), 135101 (2016).
[56] A.A. Baganich, V.I. Mikla, D.G. Semak, A.P. Sokolov, and A.P. Shebanin, phys. stat. sol. (b) **166**, 297 (1991).
[57] P.J. Carroll, and J.S. Lannin, Solid State Commun. **40**(1), 81–84 (1981).
[58] V.V. Poborchii, A.V. Kolobov, and K. Tanaka, Appl. Phys. Lett. **72**(10), 1167–1169 (1998).
[59] X. Wang, K. Kunc, I. Loa, U. Schwarz, and K. Syassen, Phys. Rev. B **74**(13), 134305 (2006).

[60] I. Caño, P. Vidal-Fuentes, L. Calvo-Barrio, X. Alcobé, J.M. Asensi, S. Giraldo, Y. Sánchez, Z. Jehl, M. Placidi, J. Puigdollers, V. Izquierdo-Roca, and E. Saucedo, ACS Appl. Mater. Interfaces **14**(9), 11222–11234 (2022).
[61] W.D. Nesse, *Introduction to Optical Mineralogy*, 4th ed (Oxford University Press, New York, NY, 2013).
[62] X.-J. Zhang, J. Zhou, and D.-J. Shu, J. Mater. Chem. A **11**(38), 20774–20785 (2023).
[63] D. Savytskii, B. Knorr, V. Dierolf, and H. Jain, J. Non-Cryst. Solids **431**, 36–40 (2016).
[64] R. Svoboda, J. Prikryl, and M. Krbal, J. Chem. Phys. **163**(10), 104502 (2025).
[65] A. Koma, Thin Solid Films **216**(1), 72–76 (1992).
[66] A. Sakai, T. Tatsumi, I. Hirosawa, H. Ono, and K. Ishida, Surf. Sci. **249**(1–3), L300–L306 (1991).
[67] J.S. Blakemore, J. Appl. Phys. **53**(10), R123–R181 (1982).
[68] R.M. Feenstra, and J.A. Stroscio, "5.3. Gallium Arsenide," in *Methods in Experimental Physics*, (Elsevier, 1993), pp. 251–276.

Supplementary Material

Solid-phase heteroepitaxy of oriented Sb_2Se_3 on GaAs for birefringent thin films

Kelly Xiao[1*], Yuejun Shen[1,2], Arturas Vailionis[3,4], Alec M. Skipper[5], Anna-Katharina Preidl[1], Aaron M. Lindenberg[1,2,6], Kunal Mukherjee[1*]

[1]*Department of Materials Science and Engineering, Stanford University, Stanford, CA, 94305, USA*

[2]*Stanford Institute for Materials and Energy Sciences, SLAC National Accelerator Laboratory, Menlo Park, CA, 94025, USA*

[3]*Stanford Nano Shared Facilities, Stanford University, Stanford, CA, 94305, USA*

[4]*Department of Physics, Kaunas University of Technology, Kaunas, Lithuania*

[5]*Institute for Energy Efficiency, University of California Santa Barbara, Santa Barbara, CA 93106, USA*

[6]*Stanford PULSE Institute, SLAC National Accelerator Laboratory, Menlo Park, CA 94025, USA*

*Corresponding Author: kellyx@stanford.edu, kunalm@stanford.edu

A. Thermal Annealing of Primary Sb-Se Film

The AFM image in Figure S1 shows an anneal at 270 °C results in a partial fraction of Sb_2Se_3 grains aligned to the GaAs [110] direction. SEM images in Figure S2 show the grain structure at different thermal anneal temperatures, in good agreement with the AFM scans for 210 – 250 °C in Figure 1 of the main text. At the lowest temperature of 210 °C, little contrast is observed indicating smooth grains. The grain structure becomes more defined approaching the higher temperatures of 230 °C, 250 °C, and 270 °C, where two distinct grain populations are observed. The first population exhibits a polygonal shape and the second exhibits a slightly elongated shape along GaAs [110]. At the highest anneal temperature of 300 °C, we observe significant surface diffusion and material evaporation that leads to large crystals (some are potentially oxides, see Raman spectra in Figure S3) and a non-continuous film.

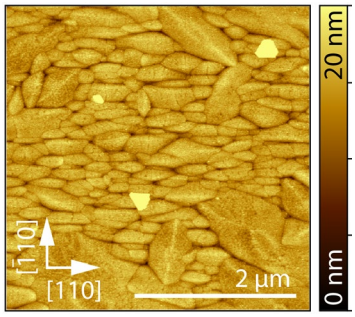

Figure S1. AFM image (4×4 µm^2) of primary Sb-Se film annealed at 270 °C for 120 s. GaAs substrate directions are drawn for reference.

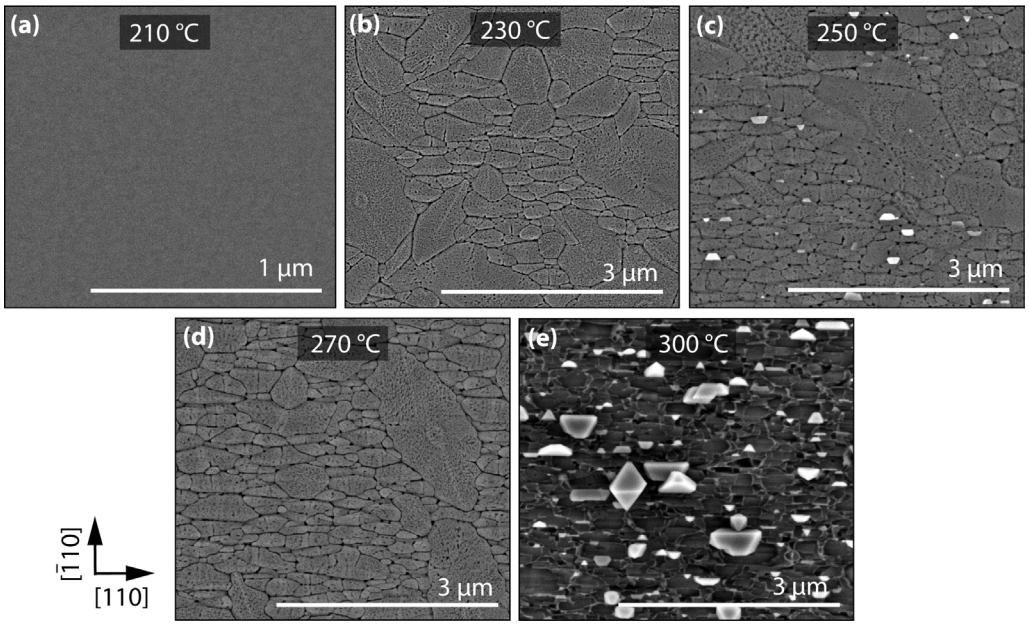

Figure S2. High-energy backscattered electron SEM micrographs of Sb-Se films separately annealed at temperatures of (a) 210 °C, (b) 230 °C, (c) 250 °C, (d) 270 °C, and (e) 300 °C, all for 120 s. Substrate directions are drawn for reference.

Seen in Figure S3, peaks assigned to secondary phases of tetragonal SeO_2 (t-SeO_2),[1,2] cubic and orthorhombic Sb_2O_3 (c-Sb_2O_3 and o-Sb_2O_3),[3] are present in the Raman spectra for films annealed at 270 °C and 300 °C. We examined multiple regions across the film and found that these secondary phases are not homogeneously distributed throughout the entire film.

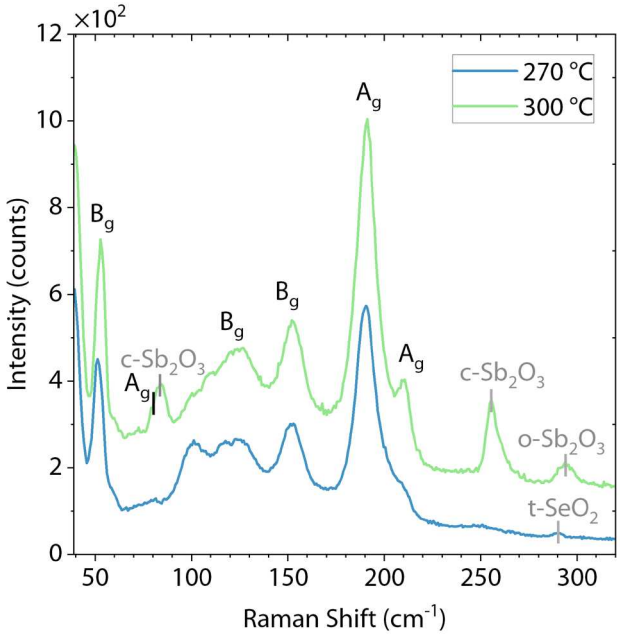

Figure S3. Raman spectra of primary Sb-Se film annealed at 270 °C and 300 °C for 120 s. The main peaks of orthorhombic Sb_2Se_3 are marked in black and secondary oxide phases in gray.

B. Testing Effects of Laser Polarization on Crystallized Morphology

We note in main text Figure 1(f)-(j), the polarization of the 633 nm laser was vertical in the sample plane, whereas in Figure 1(k), the laser polarization was horizontal with respect to the sample. These laser-crystallized spots are taken from a subset of 25 isolated spots where the vertical/horizontal polarization, dwell time (1 s to 30 min), and power (0.05-1 mW or 2-200 kW/cm^2) were varied. Sb_2Se_3 grains aligned to GaAs [110] were observed in all 25 spots.

Oriented grains are also observed using a 532 nm CW laser of unpolarized light in the sample plane across 10 additional isolated spots. We provide characterization of a ~100 μm diameter crystalline spot using conditions of ~0.5 kW/cm^2 and 120 s dwell time. Figure S4 shows representative AFM images taken from three areas of the 532 nm laser-crystallized domain. Following irradiation, aligned Sb_2Se_3 grains along the GaAs [110] direction are seen throughout the center area in Figure S4(b), near the region outer diameter in Figure S4(c), and on the edge/perimeter of the spot in Figure S4(d). Note the scan size is 10×10 μm^2 in Fig. S4(b) vs. 5×5 μm^2 in Figs. S4(c)-(d). On average, the grains are ~500 nm to 1 μm in length.

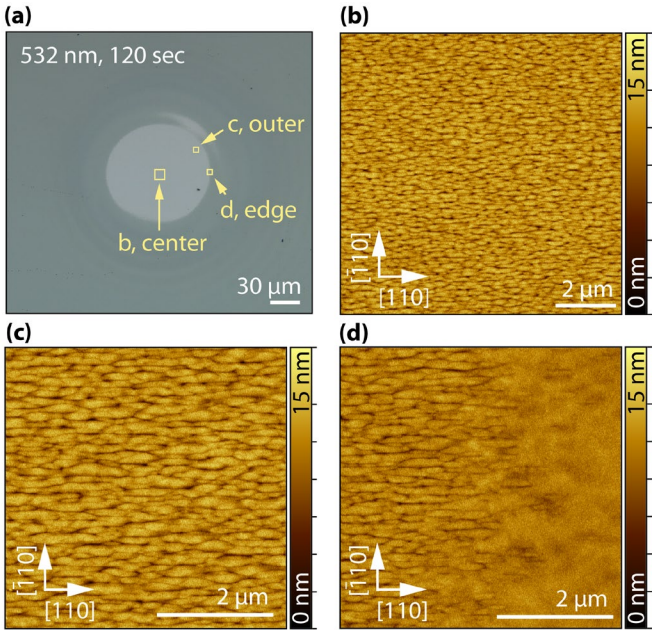

Figure S4. (a) OM image of 532 nm laser-crystallized region. (b)-(d) AFM scans showing laser-crystallized Sb_2Se_3 microstructure at the (b) center region, (c) near the outer edge, and (d) on the edge. GaAs substrate directions are drawn for reference.

C. Grazing-Incidence X-ray Scattering Analysis for Primary Sb-Se Film

Here we discuss some additional features of the grazing-incidence X-ray scattering (GIXS) diffraction patterns in main text Figure 2(d)-(e) for the primary film which has been thermally annealed and laser-crystallized.

The diffraction rings that appear in Figure 2(d) have been indexed in Figure S5 and belong to the orthorhombic *Pbnm* Sb_2Se_3 phase. One-dimensional 2θ scans were obtained by integrating scattered intensity along the detector's χ-axis within a 2D reciprocal space region excluding diffraction spots from the highly textured part of the film as well as strong substrate reflections. Because the Bragg peak positions in GIXS geometry are highly sensitive to sample height alignment, we implemented a correction procedure to account for systematic shifts in 2θ. The correction was based on three of the strongest Sb_2Se_3 reflections, namely (120), (230), and (240), which were chosen for their high intensity and wide separation in 2θ. Experimental peak positions were compared against the strain-free bulk values reported in the Powder Diffraction File JCPDS 00-015-0861, assuming that the randomly oriented polycrystalline grains in thin films were unstrained and should therefore diffract at their expected positions. The observed offsets were applied across the full diffraction pattern. This approach was necessary since even small variations in sample height alignment (from manual positioning or height drift) could otherwise introduce apparent shifts in 2θ, leading to inconsistent indexing of closely spaced reflections of the orthorhombic Sb_2Se_3 lattice. Broad peaks that exhibit insufficient signal-to-noise level or are overlapping including shoulder features were indexed with multiple possible (*hkl*).

For both main text Figures 2(d) and 2(e), we find that the diffraction patterns along GaAs $[\bar{1}10]$ exhibit several higher order reflections whereas the DP along GaAs [110] do not show peaks in the center of the frame. This effect arises from a combination of the Ewald sphere finite curvature, anisotropic broadening of the Bragg diffraction reflections due to crystal misorientation, and imaging along different directions of the Sb_2Se_3 crystal lattice.

In grazing-incidence geometry, single crystals or highly oriented monocrystalline thin films may not produce higher-order symmetrical reflections, as these do not intersect the Cu Kα Ewald sphere. However, if the crystalline grains in a thin film exhibit finite misorientation, the reciprocal lattice points broaden into arcs. These arcs can intersect the Ewald sphere, thereby giving rise to higher-order diffraction in grazing-incidence geometry. The presence of a particular symmetrical reflection when imaged along one direction, and the absence of the same reflection when imaged along another direction, therefore indicates an anisotropic mosaicity to the Sb_2Se_3 grains. Specifically, grain misorientation is greater along the GaAs $[\bar{1}10]$ direction than the [110] direction, as illustrated in Figure S6(a)-(b). We have shown that the grains exhibit mixed (*hk*0) orientations out-of-plane but are oriented in-plane via the relationship Sb_2Se_3 [001] || GaAs [110]. Thus, we see greater misorientation for the (*hk*0) planes lying perpendicular to the [001] or covalently-bonded *c*-axis, which may reflect the weak van der Waals bonding along the *a*, *b* directions of the unit cell.

The (*hk*0)-oriented grains in the film further contribute to the appearance of multiple higher-order diffraction spots. The third direction lying in-plane along GaAs [$\bar{1}$10] must be a combination of different Sb_2Se_3 [*uvw*] = [$\bar{k}h0$] directions. When the incident wavevector is along GaAs [$\bar{1}$10], these grains form a collective reciprocal lattice with a higher number of RL points intersecting the Ewald sphere.

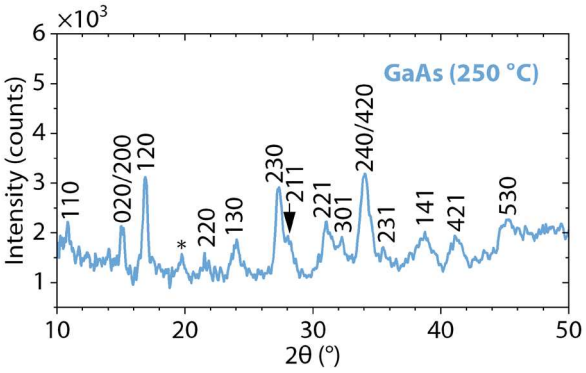

Figure S5. 2θ pattern for diffraction rings in primary Sb-Se film on GaAs after 250 °C anneal, integrated from the GIXS pattern in main text Figure 2(d). The asterisk indicates an artifact peak which does not arise from the film but from a bright isolated pixel on the camera.

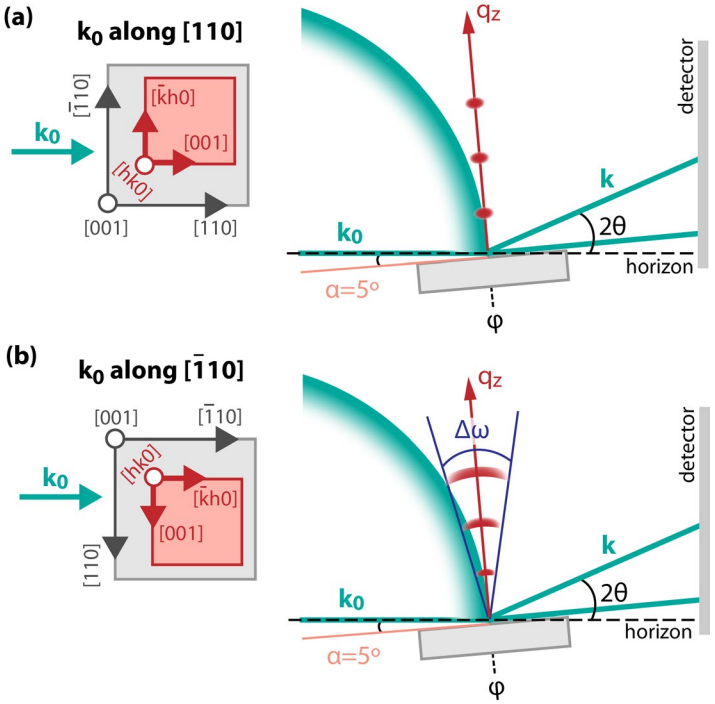

Figure S6. Schematic diagram of the grazing incidence X-ray scattering geometry (incidence angle, α, of 5°) interacting with the reciprocal lattice of a sample exhibiting preferential orientation and anisotropic mosaicity. The incident wavevector k_0 is parallel to the (a) [110] direction and (b) [$\bar{1}$10] direction of the cubic substrate. The grain misorientation Δω is shown to be larger in (b). On the left, the substrate directions and Sb_2Se_3 lattice directions (denoted in gray and red, respectively) are drawn to make the crystallographic relationships explicit.

D. Crystallization of Se-rich Films on GaAs vs. SiO_2/Si Substrates

Two additional amorphous Sb-Se films with intentionally increased Se content were grown on the same GaAs substrate and a SiO_2/Si substrate for comparison. To enter a higher Se sticking regime, we prepared films with the substrate cooled down further to thermocouple temperatures of 10-15 °C. (Thermocouple readings colder than room temperature are possible because of the liquid nitrogen cooled shroud surrounding the MBE chamber.) The BEPs, as well as Sb and Se open shutter duration, were kept the same as the primary film. The Se-rich films were thicker at approximately 200 nm, indicating the deposition rate was increased more than ~2× at the lower temperature due to greater incorporation of the incident flux, particularly Se.

AFM and SEM characterization for Se-rich recrystallized films after a 250 °C (120 s) thermal anneal are shown in Figure S7. Both films suffer from non-contacting grain boundaries, we suspect primarily due to rapid lateral diffusion of excess Se and subsequent evaporation of volatile Se. The crystalline film on the SiO_2/Si substrate shows smooth Sb_2Se_3 grains with a sinuous grain shape. This is in contrast to the film on GaAs, which has partly crystallized into high aspect ratio grains, some fraction of them aligned parallel to GaAs [110]. These grains are ~1 μm in length.

In Figure S8, we present XRD structural data for the two films. Since SiO_2 is amorphous, the SiO_2/Si control template cannot provide a seed for oriented growth of Sb_2Se_3. The out-of-plane symmetrical scan in Figure S8(a) indeed shows weak peaks arising from the film on SiO_2/Si, whereas for GaAs, the Sb_2Se_3 (100) orientation is most intense with some minor fractions of other mixed (*hk*0) reflections. Grazing incidence scattering measurements in Figures S8(b)-(c) confirm the crystallinity of both films, and reveal a two-fold structural symmetry for crystallization on GaAs in contrast to the randomly oriented polycrystalline (isotropic) film observed on SiO_2/Si. We find that the GIXS pattern on GaAs exhibits a combination of polycrystalline rings and textured spots, while the pattern on SiO_2/Si shows Debye rings only. As shown in Figure S8(b), two to three Bragg diffraction spots of the Sb_2Se_3 film crystallized on GaAs have been indexed for the two DPs along GaAs [110] and [$\bar{1}$10]. The Debye rings for both films are separately indexed in Figures S9-S10 using one-dimensional 2θ scans integrated from the respective 2D GIXS patterns. (The procedure is identical to that described in SI, Section C.)

The initial presence of Se is confirmed in Figure S11 through Raman spectroscopy. Raman spectra of the as-grown and 250 °C annealed film are shown. In the as-grown spectra, we observe a strong signal at 251 cm^{-1}, which is characteristic of amorphous-Se (a-Se).[4] A weaker intensity peak at the same wavenumber appears after annealing, becoming undetectable for the film crystallized on SiO_2/Si. This supports that Se may have evaporated from the film during the annealing process. It is most common to see the 251 cm^{-1} mode also attributed to crystalline monoclinic-Se (m-Se),[4] although we acknowledge this assignment is not definitive. There lacks a consensus on the various unstable and complex ring vs. chain structures adopted by elemental Se.[5] Due to the extreme photosensitivity of Se, it is also possible that the 251 cm^{-1} peak in the as-grown

spectra partially arises from m-Se since some slight color change was observed at the laser focus position on the sample. The rest of the vibrational modes appearing after an anneal belong to orthorhombic Sb_2Se_3 and have been previously identified in Figure 3 of the main text.

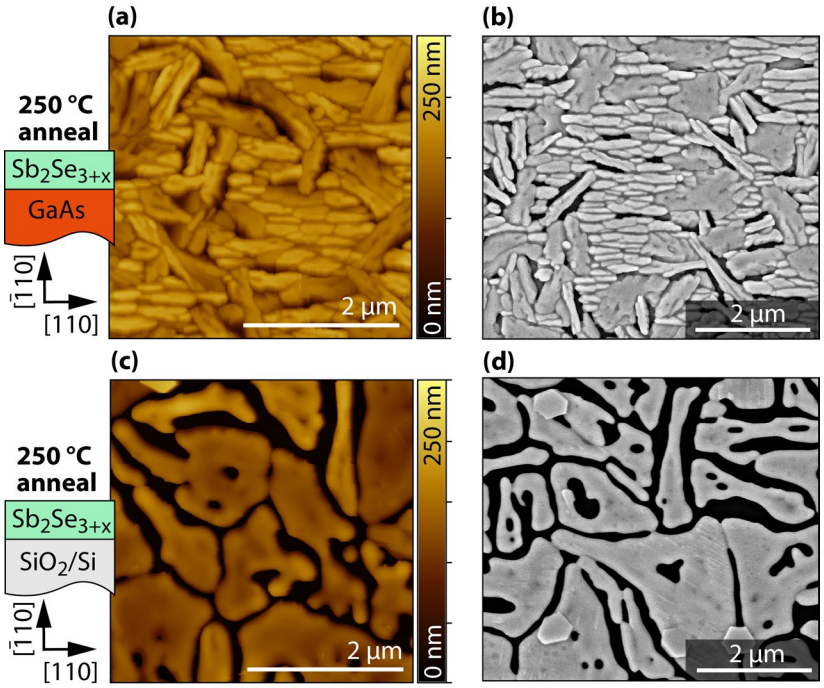

Figure S7. Morphology characterization of Se-rich Sb-Se films following a 250 °C thermal anneal. (a)-(b) AFM and secondary electron SEM images of thermally crystallized Sb-Se on GaAs. (c)-(d) SEM and AFM of thermally crystallized Sb-Se on SiO_2/Si. The layer structure and in-plane substrate directions are drawn for reference.

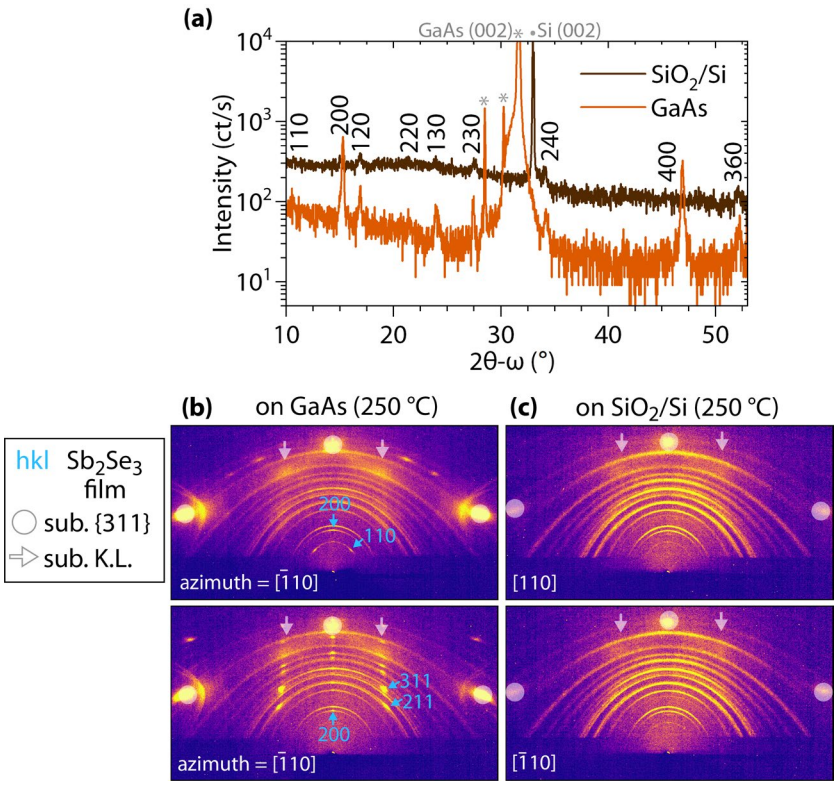

Figure S8. (a) Symmetrical out-of-plane XRD scans of Se-rich Sb-Se films on SiO_2/Si and GaAs substrates, thermally annealed at 250 °C for 120 s. Substrate peaks and related spectral reflections are denoted with an asterisk for GaAs, and a closed circle for Si. (b)-(c) GIXS patterns of Se-rich films collected along the cubic in-plane [110] and [$\bar{1}$10] azimuths of (b) GaAs substrate and (c) SiO_2/Si substrate. The substrate reflections and Kikuchi lines (K.L.) are indicated with white circles and arrows, respectively, and the Sb_2Se_3 (*hkl*) reflections are indexed in blue.

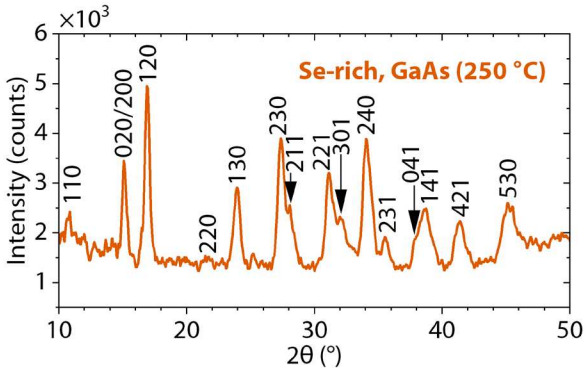

Figure S9. 2θ scan of the Se-rich Sb-Se film on GaAs after annealing at 250 °C (120 s), integrated from the GIXS pattern in Fig. S8(b).

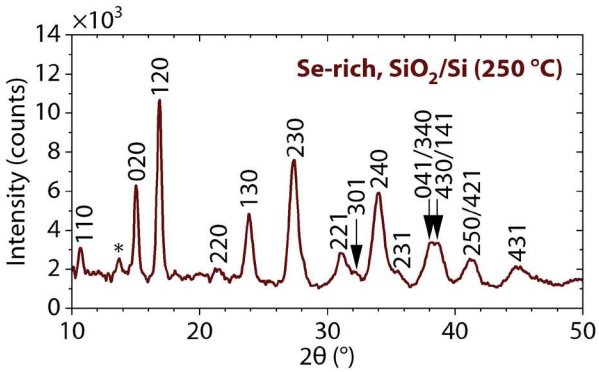

Figure S10. 2θ scan of Se-rich Sb-Se film on SiO_2/Si after thermal annealing at 250 °C (120 s), integrated from the GIXS pattern in Fig. S8(c). The asterisk indicates a secondary phase, which has been identified as a possible cubic-Sb_2O_3 (111) reflection.

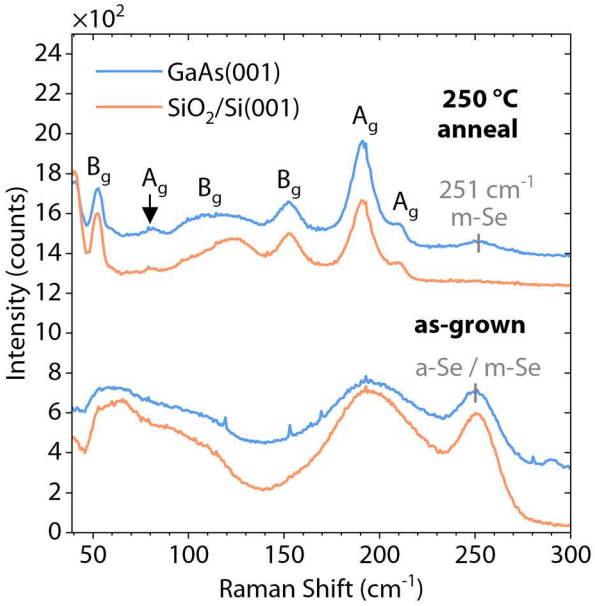

Figure S11. Raman spectra collected for Se-rich Sb-Se films in the as-grown condition and after annealing at 250 °C for 120 s. The peaks for amorphous-Se (a-Se) and monoclinic-Se (m-Se) have been highlighted.

E. Estimating Reflection in Crystallized Sb_2Se_3 Films

$\tilde{n}$ = complex refractive index
n = refractive index (real part)
k = absorption coefficient (imaginary part)
λ = wavelength
d = film thickness
$\tilde{r}$ = reflection coefficient

Standard polarized reflection

The interaction of 532 nm light on the film and substrate layer structure is illustrated in Figure S12. The refractive indices of Sb_2Se_3 and GaAs are tabulated in Table S1. We used refractive indices reported in prior work on (hk0)-oriented Sb_2Se_3 films.[6]

Sb_2Se_3 is not transparent to the visible wavelengths. In Table S2, we calculate the absorbed fraction of 532 nm by the crystalline film for a thickness, d, of 85 nm. (This thickness was estimated based on the ~90 nm thickness of the amorphous film and AFM height measurements near the crystalline-amorphous boundary in the laser-crystallized regions.) We find that the absorbed fraction is near 1 for linear polarization aligned to either in-plane axis of Sb_2Se_3. Since negligible intensity is transmitted to the film-substrate interface, the film may be effectively treated as a semi-infinite medium and back reflection can be neglected.

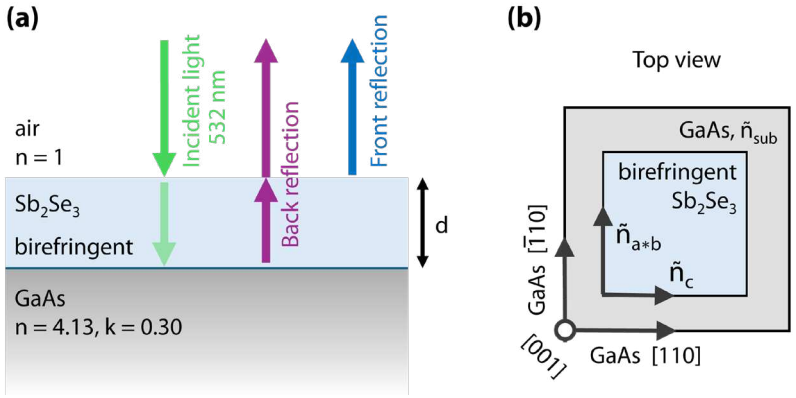

Figure S12. (a) Layer structure of Sb_2Se_3 of thickness d on a GaAs substrate. A linearly polarized 532 nm light incident on this structure can undergo two reflections, one at the film-substrate interface (back reflection) and another at the air-film interface (front reflection). (b) Top view of the Sb_2Se_3 film on GaAs, with the refractive indices labeled with respect to substrate crystallographic directions. The a*b notation represents a combination of van der Waals directions in Sb_2Se_3.

Table S1. Refractive indices for crystalline Sb_2Se_3 and GaAs at 532 nm.

Wavelength (nm)	Material	Refr. Index	Source
532	Sb_2Se_3	$n_c + ik_c$ $5.44 + 3.27\,i$ $n_{a*b} + ik_{a*b}$ $4.67 + 2.16\,i$	Xiao et al., [6]
	GaAs	$4.13 + 0.30\,i$	G.E. Jellison Jr., [7]

Table S2. Calculations of the absorbed fraction of 532 nm light by Sb_2Se_3 for the two in-plane polarizations, using a thickness, d, of 85 nm.

Wavelength (nm)	Polarization relative to Sb_2Se_3	Absorbed Fraction $A = 1 - \exp\left(-\frac{4\pi k}{\lambda} \cdot d\right)$
532	$\vec{E} \parallel c$	1.0
	$\vec{E} \parallel (a * b)$	0.99

The primary reflection therefore occurs only at the upper air-film interface. The reflectance is calculated at normal incidence for polarization aligned to the in-plane GaAs [110] vs. $[\bar{1}10]$ directions, and the resulting maximum reflectance modulation:

$$R_{110} = |\tilde{r}_{110}|^2 = \left|\frac{\tilde{n}_{air} - \tilde{n}_{c,film}}{\tilde{n}_{air} + \tilde{n}_{c,film}}\right|^2 = 0.58$$

$$R_{\bar{1}10} = |\tilde{r}_{\bar{1}10}|^2 = \left|\frac{\tilde{n}_{air} - \tilde{n}_{a*b,film}}{\tilde{n}_{air} + \tilde{n}_{a*b,film}}\right|^2 = 0.49$$

$$\therefore |\Delta R| \approx 0.15$$

Cross-polarized reflection

For white light cross-polarized microscopy, we calculate the polarization ellipse parameters of the reflected beam at an example wavelength of 532 nm. The parameters relevant to our discussion are illustrated in Figure S13a. First, the absolute phase difference, $|\delta|$, generated upon reflection at the upper air-film interface between the waves polarized along the GaAs [110] and $[\bar{1}10]$ direction is found to be very small (see calculations below). Therefore, the resulting wave is weakly elliptically polarized. We also calculate the ellipse orientation angle, ψ. When the incident polarization is 45° relative to the sample, the ellipse is rotated by 2° towards the GaAs [110] axis. The polarization ellipse is illustrated in Figure S13b.

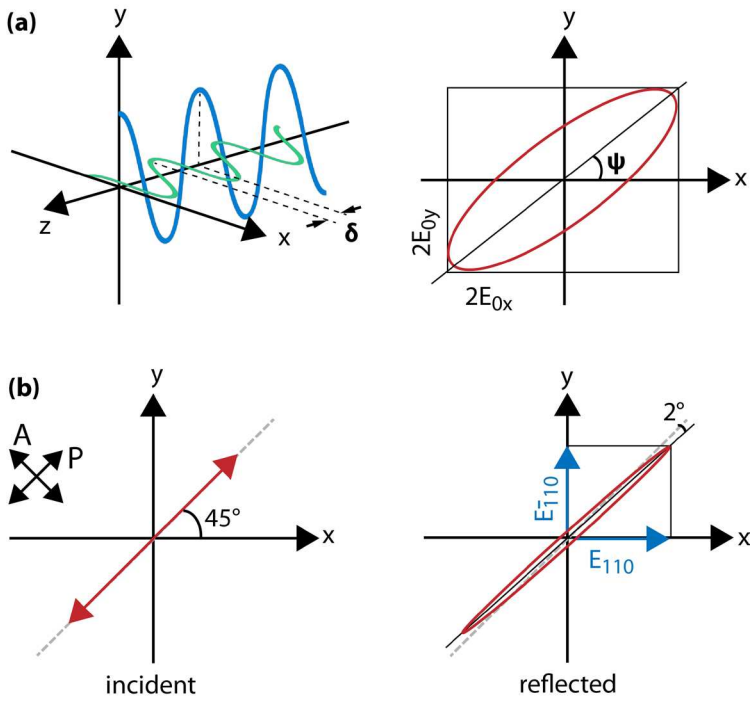

Figure S13. (a) Illustration of phase difference δ between two perpendicularly polarized waves and a polarization ellipse at orientation angle ψ. (b) Illustration of the incident light and after reflection by the in-plane anisotropic sample, when the sample is rotated to 45°.

$$
\begin{aligned}
|\delta| &= |\arg(\tilde{r}_{110}) - \arg(\tilde{r}_{\bar{1}10})| \\
&= \left|\arg\left(\frac{\tilde{n}_{air} - \tilde{n}_{c,film}}{\tilde{n}_{air} + \tilde{n}_{c,film}}\right) - \arg\left(\frac{\tilde{n}_{air} - \tilde{n}_{a*b,film}}{\tilde{n}_{air} + \tilde{n}_{a*b,film}}\right)\right| \\
&= 0.003 \text{ rad} = 0.2^{\circ}
\end{aligned}
$$

$$
\tan(2\psi) = \frac{2E_{0x}E_{0xy}}{E_{0x}^2 - E_{0y}^2}\cos\delta = \frac{2E_{110}E_{\bar{1}10}}{E_{110}^2 - E_{\bar{1}10}^2}\cos\delta = \frac{2(|\tilde{r}_{110}| \cdot |\tilde{r}_{\bar{1}10}|)}{|\tilde{r}_{110}|^2 - |\tilde{r}_{\bar{1}10}|^2}\cos\delta
$$

$\Rightarrow \psi = 42.6^{\circ}$ or $\sim 2^{\circ}$ from the reference 45° position

References

[1] A. Anderson, A. Sanders, and W. Smith, “Raman spectra of selenium dioxide at low temperatures,” J. Raman Spectrosc. **31**(5), 403–406 (2000).
[2] I.R. Beattie, N. Cheetham, T.R. Gilson, K.M.S. Livingston, and D.J. Reynolds, “Calculated and observed vibrational spectra of a linear chain, bent chain, and sheet polymer (α-bismuth pentafluoride, selenium dioxide, and tin tetrafluoride respectively),” J. Chem. Soc. A, 1910–1913 (1971).
[3] G. Mestl, P. Ruiz, B. Delmon, and H. Knozinger, “Sb_2O_3/Sb_2O_4 in reducing/oxidizing environments: an in situ Raman spectroscopy study,” J. Phys. Chem. **98**(44), 11276–11282 (1994).
[4] A.H. Goldan, C. Li, S.J. Pennycook, J. Schneider, A. Blom, and W. Zhao, “Molecular structure of vapor-deposited amorphous selenium,” J. Appl. Phys. **120**(13), 135101 (2016).
[5] W. Lu, Z. Li, M. Feng, L. Zheng, S. Liu, B. Yan, J.-S. Hu, and D.-J. Xue, “Structure of Amorphous Selenium: Small Ring, Big Controversy,” J. Am. Chem. Soc. **146**(9), 6345–6351 (2024).
[6] K. Xiao, V. Tara, P.D. Reddy, J.E. Meyer, A.M. Skipper, R. Chen, L.J. Nordin, A. Majumdar, and K. Mukherjee, “Heteroepitaxial growth of highly anisotropic Sb_2Se_3 films on GaAs,” Mater. Horiz., **12**, 5829–5838 (2025).
[7] G.E. Jellison, “Optical functions of GaAs, GaP, and Ge determined by two-channel polarization modulation ellipsometry,” Optical Materials **1**(3), 151–160 (1992).